

Lithium Niobate: Summary of Physical Properties and Crystal Structure

R. S. Weis and T. K. Gaylord

School of Electrical Engineering, Georgia Institute of Technology, Atlanta, GA 30332, USA

Received 25 February 1985/Accepted 24 March 1985

Abstract. Ferroelectric lithium niobate (LiNbO_3) is widely used in integrated and guided-wave optics because of its favorable optical, piezoelectric, electro-optic, elastic, photoelastic, and photorefractive properties. However, detailed summaries of its pertinent physical properties and crystal structure are not readily available. In this tutorial paper, the important tensor physical properties and their mathematical descriptions are compiled and presented. The essential features of the structure of lithium niobate, including its hexagonal and rhombohedral unit cells, are illustrated and the principal (Cartesian) axes used in the description of the anisotropic properties are specified relative to the crystal structure. Errors in property coefficient values and structure information that have been propagated in the literature are corrected.

PACS: 78.20.-e, 42.70.Fh

Lithium niobate (LiNbO_3) is centrally important in integrated and guided-wave optics. It is a human-made dielectric material that does not exist in nature. It was first discovered to be ferroelectric in 1949 [1]. Lithium niobate was synthesized in single crystal form and investigated in detail at Bell Laboratories. This resulted in a cornerstone series of five papers published in 1966 [2–6] about the structure and properties of the material. It is now one of the most widely used electro-optic materials. This ferroelectric material has a trigonal crystal structure and is characterized by large pyroelectric, piezoelectric, electro-optic, and photoelastic coefficients. Lithium niobate is naturally birefringent. It has useful acoustic wave properties and a relatively large acousto-optic figure-of-merit. In addition, it exhibits a very strong bulk photovoltaic effect. This effect causes efficient charge migration within the material and in combination with the material's linear electro-optic effect, can produce a significant photorefractive effect (optically induced refractive-index changes).

This richness of large-magnitude physical effects has caused lithium niobate to become widely used in applications such as acoustic wave transducers, acoustic delay lines, acoustic filters, optical amplitude modulators, optical phase modulators, second-harmonic

generators, Q -switches, beam deflectors, phase conjugators, dielectric waveguides, memory elements, holographic data processing devices, and others.

Although lithium niobate is important in numerous broad areas of technological significance, the details of its physical properties and crystal structure are not readily available in textbooks. Instead, a large number of research papers must be studied in considerable detail to gain a definitive insight into its properties and structure. It is the purpose of this paper to gather together, in one place, basic information about the physical properties and crystal structure of lithium niobate. In addition, numerous errors in coefficient values that have been propagated in the literature and erroneous structure information are corrected.

1. General Characteristics

Lithium niobate's structure at temperatures below its ferroelectric Curie temperature (approximately 1210°C) consists of planar sheets of oxygen atoms in a distorted hexagonal close-packed configuration. The octahedral interstices formed in this structure are one-third filled by lithium atoms, one-third filled by niobium atoms, and one-third vacant. In the $+c$ direction, the atoms occur in the interstices in the

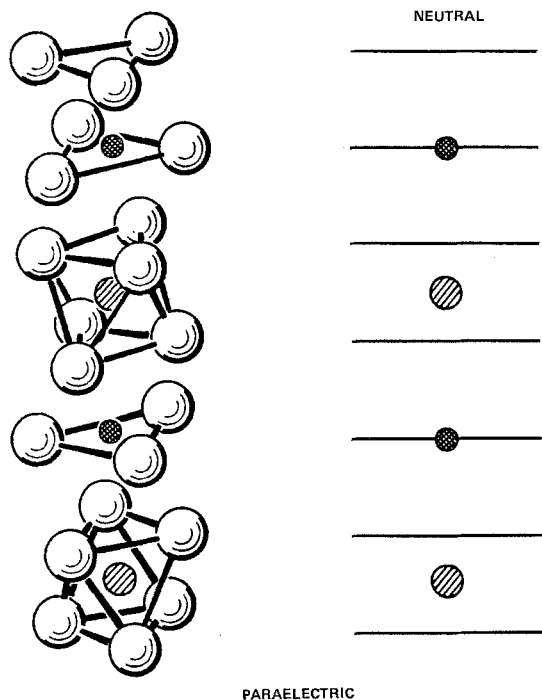


Fig. 1. Positions of the lithium atoms (double cross-hatched circles) and the niobium atoms (single cross-hatched circles) with respect to the oxygen octahedra in the paraelectric phase ($T \geq T_c$) of lithium niobate. The positions of the lithium atoms are actually equally probable to be either above or below the oxygen layers by 0.37 Å. The lithium atoms shown are in the average position – in the oxygen layer. The horizontal lines in the diagram on the right represent the oxygen layers. After [6, 7]

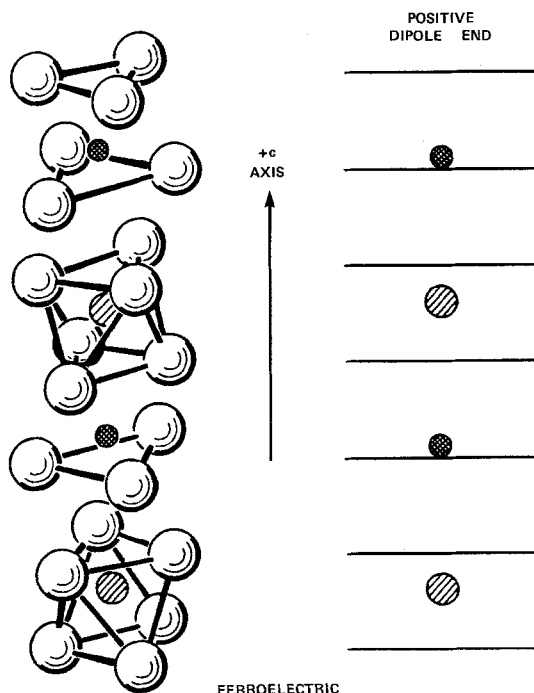


Fig. 2. Positions of the lithium atoms and niobium atoms with respect to the oxygen octahedra in the ferroelectric phase ($T < T_c$) of lithium niobate. After [6, 7]

following order: ..., Nb, vacancy, Li, Nb, vacancy, Li, ... [4].

In the paraelectric phase above the Curie temperature, the Li atoms lie in an oxygen layer that is $c/4$ away from the Nb atom, and the Nb atoms are centered between oxygen layers. These positions make the paraelectric phase non-polar [6]. As the temperature decreases from the Curie temperature, the elastic forces of the crystal become dominant and force the lithium and niobium ions into new positions. The charge separation resulting from this shift of ions relative to the oxygen octahedra causes LiNbO_3 to exhibit spontaneous polarization at temperatures below 1210 °C. Thus, LiNbO_3 belongs to the broad class of displacement ferroelectrics. Barium titanate (BaTiO_3) and lithium tantalate (LiTaO_3) are other examples of displacement ferroelectrics.

The positions of the lithium and niobium atoms in both the paraelectric and ferroelectric phases are shown in Figs. 1 and 2. Because lithium niobate's Curie temperature is so high, the remainder of this paper will discuss only the ferroelectric phase.

2. Crystal Structure

2.1. Classification

In the ferroelectric phase a LiNbO_3 crystal exhibits three-fold rotation symmetry about its c axis. Thus, it is a member of the trigonal crystal system. In addition, it exhibits mirror symmetry about three planes that are 60° apart and intersect forming a three-fold rotation axis as shown in Fig. 3. These two symmetry operations then classify LiNbO_3 as a member of the $3m$ point group (C_{6v} in Schönflies notation) [8]. It also belongs to the $R3c$ space group [4]. In the trigonal system, two quite different unit cells can be chosen: hexagonal or rhombohedral. The conventional hexagonal unit cell in LiNbO_3 contains six formula weights, while the conventional rhombohedral unit cell contains only two formula weights.

2.2. Hexagonal Unit Cell

Figure 4 shows the conventional hexagonal unit cell for LiNbO_3 . In this unit cell, the c axis is defined as the axis about which the crystal exhibits three-fold rotation symmetry [9]. The standard method of determining the sense of the c axis is to compress the crystal in the c axis direction. The $+c$ axis is defined as being directed out of the c face that becomes negative upon compression [9]. A second method to determine the $+c$ axis is to cool the crystal. The $+c$ axis is directed out of the c face that becomes positive upon cooling [10]. Both of these methods can be understood

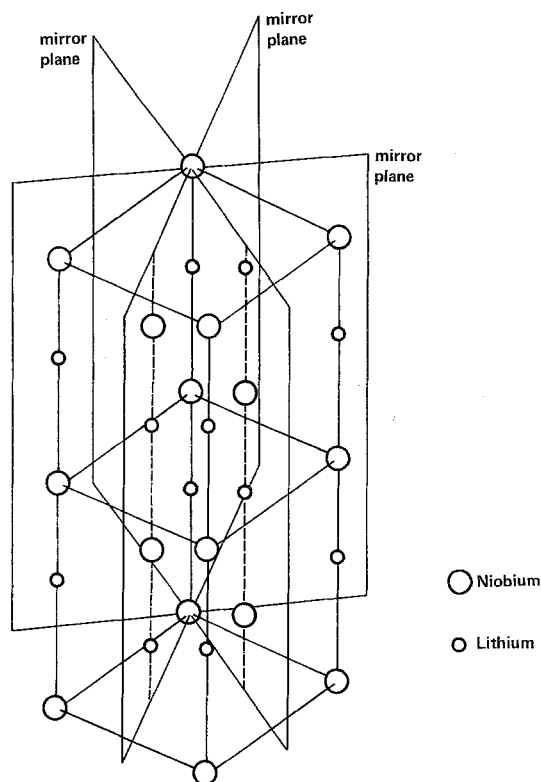


Fig. 3. Three mirror plane symmetry elements associated with lithium niobate ($3m$ crystal class)

qualitatively by considering the movement of the Li and Nb ions relative to the oxygen octahedra. The undisturbed positions of the Li and Nb ions relative to the oxygen octahedra at room temperature are depicted in Fig. 2. Upon compression the ions move closer to their centered (paraelectric) positions with respect to the oxygen layers thereby reducing the net polarization and leaving an excess amount of negative compensating charge on the $+c$ face, causing the $+c$ face to become negative. Conversely, when the crystal is cooled, the elastic forces pull the Li and Nb ions further from the corresponding oxygen layers, increasing the net polarization along the c axis and producing a deficiency of negative compensating charge on the $+c$ face, thus causing the $+c$ face to become positively charged. A third method of determining the polarity of the c axis is by observation of the "terracing" that appears on a cleavage plane. A cleave started by a scribe mark from the $+c$ direction exhibits a double row of terraces upon cleaving. However, cleaves started with a short, light scribe mark from the $-c$ direction exhibit only a single row of terraces upon cleaving. Details of this method were given in [11]. The three equivalent a axes (a_1, a_2, a_3) of the conventional hexagonal unit cell are 120° apart and lie in a plane normal to the c axis. According to the adopted

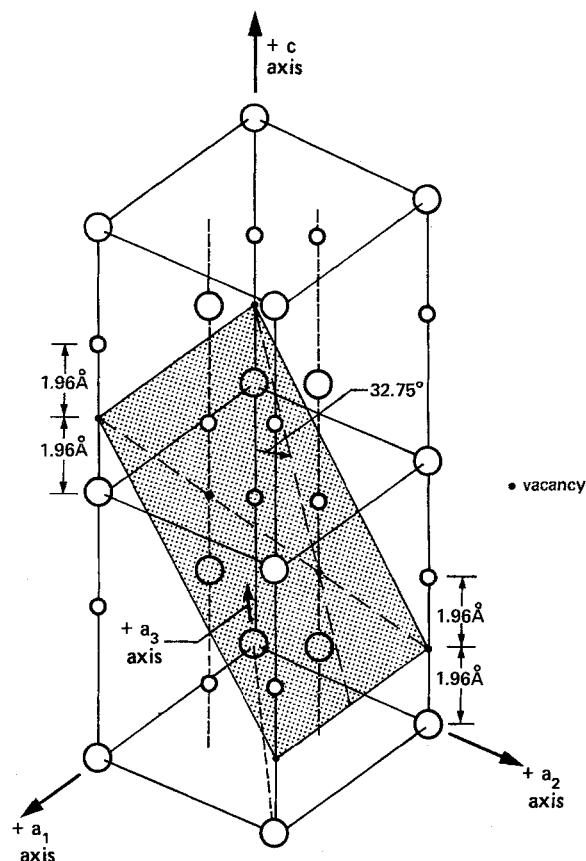


Fig. 4. Conventional hexagonal unit cell of lithium niobate with hexagonal axes (a_1, a_2, a_3, c) and cleavage plane ($01\bar{1}2$) indicated. The angle between the cleavage plane and the $+c$ axis has been both measured and calculated to be 32.75° . Vacancies are indicated only on the cleavage plane

convention, these axes are chosen to be perpendicular to the mirror planes of symmetry [9]. The axes of the conventional hexagonal unit cell are shown in Fig. 4. Figure 5 shows the hexagonal unit cell with the positional coordinates of the lithium and niobium atoms indicated. A corresponding hexagonal unit cell diagram with the interatomic distances indicated is presented in Fig. 6. The distances 3.765, 3.054, 3.010, 3.381, 3.922, 5.148, and 13.863 Å were determined directly by x-ray diffraction techniques [4], while the other distances were geometrically derived from the x-ray-measured distances. The sum of the interatomic distances along the c axis ($2 \times 3.922 \text{ Å} + 2 \times 3.010 \text{ Å}$) correlates with the c axis value of 13.863 Å determined by x-ray diffraction techniques. It should be noted that the Nb-Li distance of 3.054 Å is not perpendicular to the c axis, as stated in [4]. In terms of the mass density, the volume of the hexagonal unit cell is $(MW)(n)/(qN_0)$, where MW is the molecular weight (147.842), n is the number of molecules per unit cell ($n=6$ for the conventional hexagonal unit cell), q is the

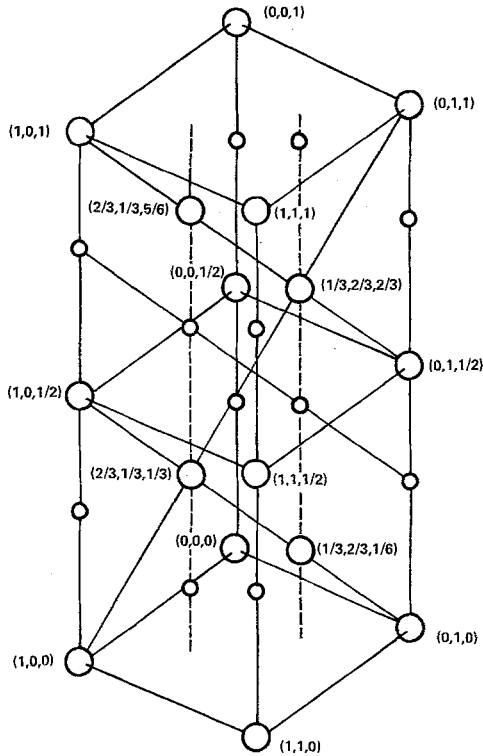


Fig. 5. Hexagonal unit cell of lithium niobate with positional coordinates of lithium and niobium atoms indicated [4]

mass density ($4.628 \times 10^3 \text{ kg/m}^3$), and N_0 is Avogadro's number. In terms of lattice parameters, the volume of the hexagonal unit cell is $3^{1/2} a_H^2 c/2$. Using $c = 13.863 \text{ \AA}$, the value of a_H is therefore calculated to be 5.150 \AA in good agreement with the value of $a_H = 5.148 \text{ \AA}$ cited in [4].

2.3. Cleavage Planes

Lithium niobate cleaves naturally along the $\{01\bar{1}2\}$ planes [10]. Because lithium niobate exhibits three-fold rotational symmetry there are three cleavage planes ($01\bar{1}2$), ($\bar{1}012$), and ($1\bar{1}02$). The $(01\bar{1}2)$ plane is shown shaded in Fig. 4. The natural cleavage can be qualitatively understood by noting that the vacant octahedral sites lie in this plane which is located midway between a plane of lithium atoms and a plane of niobium atoms. It is reasonable to assume that cleavage occurs at this vacancy plane because the bonding perpendicular to this plane between these positive ions is weak. The angle between the $+c$ axis and the cleavage plane was measured by Kaminow et al. to be 32.75° [11] in agreement with the calculated value of 32.7502° .

2.4. Rhombohedral Unit Cell

As previously mentioned, crystals that belong to the trigonal crystal system, can be structurally character-

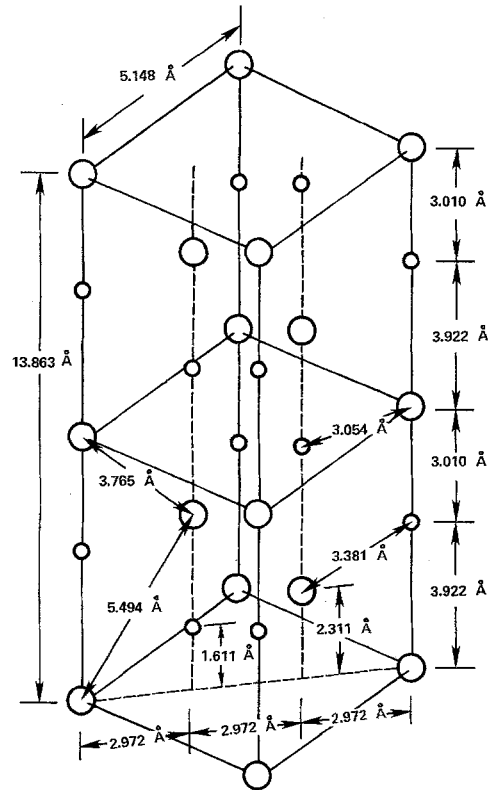


Fig. 6. Hexagonal unit cell of lithium niobate with interatomic distances and axis lengths indicated. The following were determined by x-ray diffraction techniques and reported in [4]: 3.765 , 3.054 , 3.010 , 3.381 , and 3.922 \AA . Two values cited in [4] and attributed to W. L. Bond are: 13.863 and 5.148 \AA . The remaining values were calculated geometrically from the values reported in [4]

ized by either a hexagonal or rhombohedral unit cell. Both cells are shown together in Fig. 7 for the LiNbO_3 structure. The rhombohedral parameters may be determined from the hexagonal dimensions using

$$a_R = (3a_H^2 + c^2)^{1/2}/3, \quad (1)$$

$$\alpha = 2 \sin^{-1} \{3/2[3 + (c/a_H)^2]^{1/2}\}.$$

For lithium niobate, these equations predict $a_R = 5.494 \text{ \AA}$ and $\alpha = 55.867^\circ$ [4]. These parameters are illustrated in Fig. 8.

2.5. Stoichiometry

When Abrahams et al. [4–6] accurately determined the crystal structure in 1966, the large possible deviations in stoichiometry in the lithium niobate system were generally unknown [13]. The dependence of the lattice parameters on the exact composition of lithium niobate was established by Lerner et al. [14] in 1968. A very reliable and accurate indicator of a particular sample's stoichiometry is its Curie temperature [15, 16]. Comparison of the measured Curie temperature with Curie temperatures of known stoichiometry

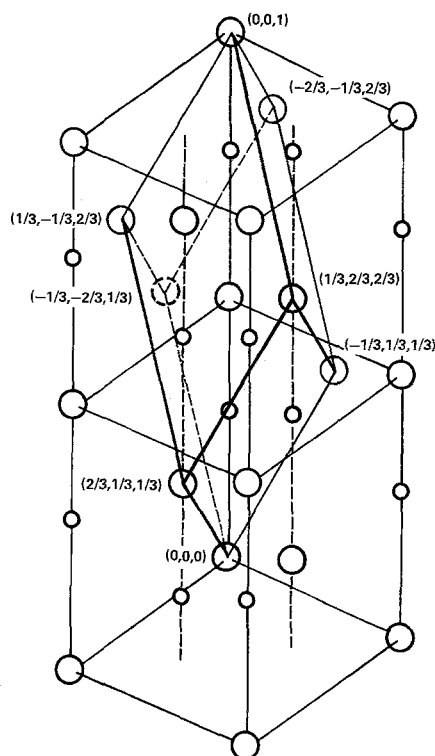


Fig. 7. Conventional rhombohedral unit cell of lithium niobate shown with respect to the hexagonal unit cell. After [12]

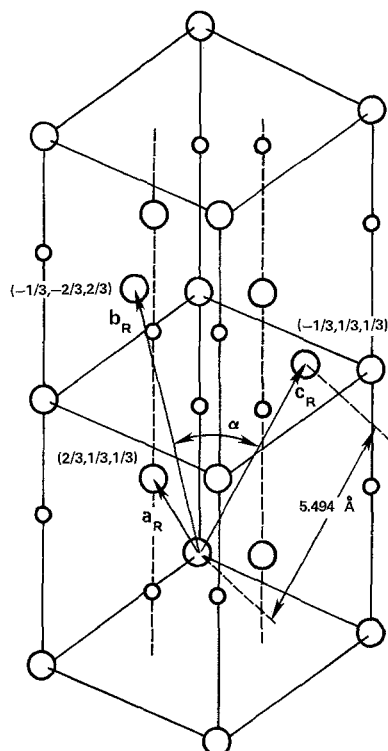


Fig. 8. Rhombohedral unit cell axes (a_R , b_R , c_R) and angle (α) between axes; $\alpha = 55.867^\circ$.

uniquely determines the chemical composition of the sample.

A wealth of information on the chemistry of the lithium niobate system is contained in [13] and it may be consulted for further details on the effects of stoichiometry.

2.6. Thermal Expansion

The thermal expansion characteristics of the lattice parameters of lithium niobate were partially explained in terms of crystal structure by Megaw [17]. The increasing tilt of the oxygen octahedra with increasing temperature is responsible for the nearly linear thermal expansion of the hexagonal lattice parameter a observed by Sugii et al. [18]. The contraction of the hexagonal lattice parameter c in the temperature range 600° to 1000°C is due to the decreasing edge length of the octahedra as the Nb ions move toward their paraelectric positions [17]. Experimental linear thermal expansion coefficients have been tabulated in [19] and [20].

3. Physical Properties

3.1. Coordinate System for Tensor Properties

The coordinate system used to describe the physical tensor properties of lithium niobate is neither hexa-

gonal nor rhombohedral but rather a Cartesian x , y , z system. The accepted convention for relating the hexagonal axes to the x , y , z principal axes [9] is described here. The z axis is chosen to be parallel to the c axis. The x axis is chosen to coincide with any of the equivalent a_H axes. After the x and the z axes are selected, the y axis is chosen such that the system is right handed. Thus, the y axis must lie in a plane of mirror symmetry. The sense of the z axis is, of course, the same as that of the c axis. The sense of the y axis is determined in a manner similar to that described for the z axis. Upon compression the $+y$ face becomes negatively charged. The sense of the x direction, however, cannot be determined in this way because it is perpendicular to a mirror plane. Any charge movement on one side of the plane is "mirrored" on the opposite side, hence the x faces do not become charged.

Figure 9 illustrates both the standard convention and a secondary convention for choosing the x and y principal axes within the hexagonal unit cell in LiNbO_3 . Figure 10 shows the standard convention orientation for the x , y , and z principal axes with respect to the crystal boule [9]. When working with tensors the x , y , z principal axes are often referred to as the x_1 , x_2 , and x_3 axes, respectively.

Suppliers of lithium niobate crystals [21] furnish pieces that are commonly in the form of plates. These slices may be designated x -cut, y -cut, or z -cut, corre-

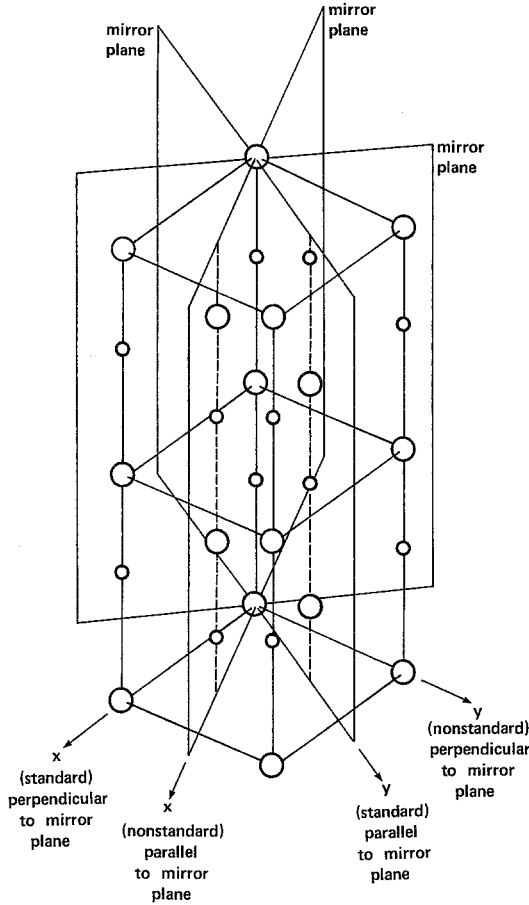


Fig. 9. Standard orientation of the x , y , and z principal axes used to describe tensor physical properties in lithium niobate

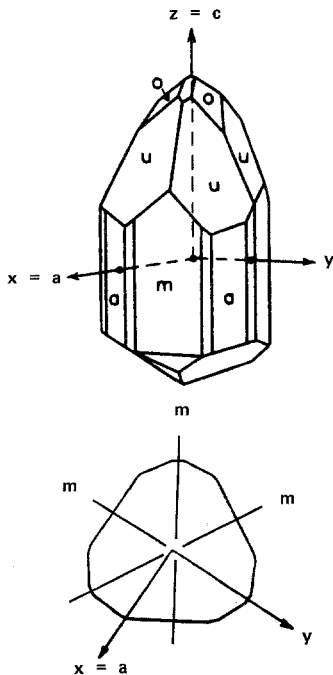


Fig. 10. Standard orientation of the x , y , and z principle axes relative to the crystal boule for lithium niobate. After [9]

spending, respectively, to the x , y , or z axes being normal to the large area surfaces. A second letter is often added to the plate orientation description according to the IRE standard [9]. The second letter indicates the direction of the longest dimension of the rectangular plate [9]. Thus, an xy -cut plate is an x -cut plate with its longest dimension parallel to the y axis. Similarly, crystal plates can be xz -cut, yx -cut, yz -cut, zx -cut, or zy -cut.

3.2. Pyroelectric Effect

A pyroelectric solid exhibits a change in spontaneous polarization as a function of temperature. The relationship between the change in temperature, ΔT , and the change in spontaneous polarization, $\Delta \mathbf{P}$, is linear and can be written as $\Delta \mathbf{P} = \hat{\rho} \Delta T$ where $\hat{\rho}$ is the pyroelectric tensor. In tensor component form this may be written as $\Delta P_i = \rho_{ij} \Delta T$. In lithium niobate this effect is due to the movement of the lithium and niobium ions relative to the oxygen layers. Since the Li and Nb ions move only in a direction parallel to the c -axis, the pyroelectric tensor is of the form,

$$\rho_i = \begin{bmatrix} 0 \\ 0 \\ \rho_3 \end{bmatrix}, \quad (2)$$

where $\rho_3 = -4 \times 10^{-5} \text{ C}/(\text{K} - \text{m}^2)$ [22]. Note that the negative value of ρ_3 indicates, that upon cooling, the $+c$ crystal face will become more positively charged as previously discussed.

3.3. Permittivity

The relationship between electric flux density \mathbf{D} and electric field \mathbf{E} is linear and can be written as $\mathbf{D} = \tilde{\epsilon} \mathbf{E}$, where $\tilde{\epsilon}$ is the second-rank permittivity tensor. In tensor component form this relationship may be expressed as

$$D_i = \sum_j \epsilon_{ij} E_j, \quad (3)$$

where $i, j = x, y, \text{ or } z$. It can be shown through a thermodynamic conservation of energy argument that only the diagonal elements of the permittivity tensor are non-zero for non-gyrotropic materials. Furthermore, since the lithium niobate crystal is symmetric about the c axis, the permittivity is the same for any electric field direction in the plane perpendicular to the c axis. Thus, the permittivity tensor can be represented by the 3×3 matrix,

$$\epsilon_{ij} = \begin{bmatrix} \epsilon_{11} & 0 & 0 \\ 0 & \epsilon_{11} & 0 \\ 0 & 0 & \epsilon_{33} \end{bmatrix}. \quad (4)$$

Table 1. Relative permittivity coefficients

$\epsilon_{11}^T/\epsilon_0$	$\epsilon_{33}^T/\epsilon_0$	$\epsilon_{11}^S/\epsilon_0$	$\epsilon_{33}^S/\epsilon_0$	T_c [°C]	Ref.
85.2	28.7	44.3	27.9	1165	[23]
84	30	44	29	—	[22]
84.6	28.6	—	—	—	[24]
—	—	43.9	23.7	—	[25]
84.1	28.1	46.5	27.3	—	[26]

Table 2. Refractive indices

λ [nm]	Laser	Stoichiometric ($T = 25^\circ\text{C}$) [30]		Congruently melting ($T = 24.5^\circ\text{C}$) [29]	
		n_o	n_E	n_o	n_E
441.6	He–Cd	2.3906	2.2841	2.3875	2.2887
457.9	Ar	2.3756	2.2715	2.3725	2.2760
465.8	Ar	2.3697	2.2664	2.3653	2.2699
472.7	Ar	2.3646	2.2620	2.3597	2.2652
476.5	Ar	2.3618	2.2596	2.3568	2.2627
488.0	Ar	2.3533	2.2523	2.3489	2.2561
496.5	Ar	2.3470	2.2468	2.3434	2.2514
501.7	Ar	2.3435	2.2439	2.3401	2.2486
514.5	Ar	2.3370	2.2387	2.3326	2.2422
530.0	Nd	2.3290	2.2323	2.3247	2.2355
632.8	He–Ne	2.2910	2.2005	2.2866	2.2028
693.4	Ruby	2.2770	2.1886	2.2726	2.1909
840.0	GaAs	2.2554	2.1703	2.2507	2.1719
1060.0	Nd	2.2372	2.1550	2.2323	2.1561
1150.0	He–Ne	2.2320	2.1506	2.2225	2.1519

Permittivity is often normalized in terms of the permittivity of vacuum (ϵ_0). The dimensionless constant ϵ_{ij}/ϵ_0 is called relative permittivity or the dielectric constant. When measuring permittivity, mechanical constraints imposed on the crystal are important. If the crystal is free (unclamped), the stress in the crystal is zero; if the crystal is rigidly held (clamped), the strain in the crystal is zero. Capacitance measurements at very low frequencies are used to determine the unclamped values of permittivity (ϵ^T) [23–25]. Capacitance measurements at frequencies well above the mechanical resonance can be used to determine directly the clamped values of permittivity (ϵ^S) [23]. The clamped values can also be determined indirectly from acoustic phase velocity measurements [24]. Measured values of relative permittivity are listed in Table 1. The differences between the measured values may be due to stoichiometric differences between samples [28]. The stoichiometries of the samples are indicated in the table by the value of T_c , the Curie temperature. The temperature behavior of the permittivity of lithium niobate was described in [24]. At optical frequencies the permittivity of a material is usually described by the refractive index.

The refractive indices of lithium niobate have been measured and compiled for two chemical compositions: stoichiometric and congruently melting. A crystal of congruently melting composition is one which grows from a melt of the same composition. For lithium niobate, the congruently melting composition corresponds to a Li/Nb mole ratio of 0.946 [14, 15, 29]. The refractive indices presented in [29, 30] have been linearly interpolated to standard laser wavelengths and are presented in Table 2. More recently measured values [31] confirm those in [29]. The temperature behavior of the refractive indices for stoichiometric and congruently melting compositions can be found in [30] and [31], respectively. A temperature-dependent dispersion relation for the congruently melting composition can be found in [32].

The birefringence of a material is defined as the difference ($n_E - n_o$), where n_E is the principal extraordinary refractive index and n_o is the principal ordinary refractive index. The negative birefringence of lithium niobate can be understood qualitatively by considering the effect of the atomic dipoles that are induced by an applied electric field. When a field is applied, the negatively charged electrons and positively charged nucleus separate and produce an electric dipole. If the induced dipoles produce a net decrease of the field at their neighboring atoms, then the dielectric susceptibility χ_e is decreased. This results in a smaller relative permittivity since $\epsilon/\epsilon_0 = 1 + \chi_e$. Likewise if the induced dipoles produce a net increase in the field at their neighboring atoms, the dielectric susceptibility and the relative permittivity are correspondingly increased. The polarizing and depolarizing effects of the induced oxygen dipoles on their nearest-neighbor atoms produce the dominant contribution to the dielectric susceptibility in lithium niobate. If the applied electric field is parallel to the optic axis, the induced oxygen dipoles have a net depolarizing effect on their nearest oxygen neighbors. But if the applied electric field is perpendicular to the optic axis, the induced oxygen dipoles have a net polarizing effect on their nearest oxygen neighbors. Therefore χ_e parallel to the optic axis is less than χ_e perpendicular to the optic axis. Thus, lithium niobate's principal extraordinary refractive index [$n_E = (\epsilon_{33}/\epsilon_0)^{1/2}$] is less than its ordinary refractive index [$n_o = (\epsilon_{11}/\epsilon_0)^{1/2}$].

3.4. Piezoelectric Effect

A piezoelectric solid exhibits an induced polarization with applied stress. The relationship between polarization and stress is linear and may be written as $\mathbf{P} = \tilde{d}\tilde{\sigma}$, where the vector \mathbf{P} is the induced polarization, $\tilde{\sigma}$ is the second-rank stress tensor, and \tilde{d} is the third-rank piezoelectric tensor. In tensor component form, the

piezoelectric effect may be expressed

$$P_i = \sum_{j,k} d_{ijk} \sigma_{jk}, \quad (5)$$

where $i, j, k = x, y, z$. It can be shown through general thermodynamic arguments that

$$\sigma_{jk} = \sigma_{kj}. \quad (6)$$

Thus, the d_{ijk} tensor contains only 18 independent elements and can be written as a 3×6 matrix. Customarily the jk subscripts are reduced to a single subscript using the substitutions

$$\begin{aligned} jk=11 &\Rightarrow 1, & jk=22 &\Rightarrow 2, \\ jk=33 &\Rightarrow 3, & jk=23, 32 &\Rightarrow 4, \\ jk=31, 13 &\Rightarrow 5, & jk=12, 21 &\Rightarrow 6. \end{aligned} \quad (7)$$

Since the lithium niobate crystal possesses $3m$ point group symmetry, all tensors describing the physical properties of lithium niobate must have at least that symmetry. They can have more symmetry than the crystal structure but they can have no less symmetry than the crystal structure. This basic principle was first asserted by Neumann in 1833. Neumann's principle can not be properly applied to the reduced subscript matrix but rather must be applied to the original tensor [8, 33].

The application of Neumann's principle to the d_{ijk} tensor followed by the use of the reduced-subscript notation gives

$$d_{ijk} = \begin{bmatrix} 0 & 0 & 0 & 0 & d_{15} & -2d_{22} \\ -d_{22} & d_{22} & 0 & d_{15} & 0 & 0 \\ d_{31} & d_{31} & d_{33} & 0 & 0 & 0 \end{bmatrix}. \quad (8)$$

Note that $d_{15} = d_{24}$, $d_{22} = -d_{21} = (-d_{16})/2$, and $d_{31} = d_{32}$. Thus the piezoelectric effect in lithium niobate can be described by four independent coefficients d_{15} , d_{22} , d_{31} , and d_{33} . Measured values for these quantities are presented in Table 3. Valuable bibliographic information for the tables presented was obtained from [34]. Unfortunately, some of the parameter values in [34] were found to be in error after comparison with the original sources.

The fact that both d_{22} and d_{33} are positive is due to the convention discussed previously for determining the senses of the y (x_2) and z (x_3) axes. The determination

of these piezoelectric coefficients is often based on taking differences of ultrasonic wave velocities of comparable magnitudes, thus they are subject to rather large percentage errors (especially d_{33}) [35]. However, the linear hydrostatic coefficient, d_h , has been measured to within 1.5% [35]. For crystals possessing $3m$ symmetry, $d_h = 2d_{31} + d_{33}$. The magnitudes of d_h predicted by values from [23, 24] and [25] are 4.0, 4.3, and $14.5 (\times 10^{-12} \text{ C/N})$, respectively. However, a direct measurement by hydrostatic loading determined d_h to be $(6.31 \pm 0.014) \times 10^{-12} \text{ C/N}$ [35]. Subsequent hydrostatic measurements of d_h for nine samples from five different suppliers [36] showed excellent agreement with the value reported in [35].

3.5. Converse Piezoelectric Effect

A piezoelectric solid also exhibits a change in shape (strain) with an applied electric field. This is called the converse piezoelectric effect. It can be shown through a thermodynamic argument that the coefficients connecting the induced strain and the applied electric field are identical to those connecting the induced polarization and the applied stress in the direct piezoelectric effect [Ref. 33, p. 115]. In tensor component form, the converse piezoelectric effect may be expressed

$$S_{jk} = \sum_i d_{ijk} E_i \quad (9)$$

where S_{jk} is the second-rank strain tensor.

3.6. Linear Electro-Optic Effect (Pockels Effect)

The linear electro-optic effect (Pockels effect) is manifested in a solid by a change in the refractive index as a function of applied electric field. The relationship between the refractive index and the applied electric field can be written

$$\Delta(1/n^2)_{ij} = \sum_k r_{ijk} E_k, \quad (10)$$

where $\Delta(1/n^2)_{ij}$ is the second-rank tensor describing the change in relative permittivity, E_k is the k -th component of the electric field, a vector, and $i, j, k = x, y, z$. Thus r_{ijk} the linear electro-optic coefficient tensor, is a third-rank tensor with 27 elements. Using the properties of the index ellipsoid (or indicatrix) [Ref. 33, p. 243 and 246] it can be shown that

$$\Delta(1/n^2)_{ij} = \Delta(1/n^2)_{ji}. \quad (11)$$

Thus, the r_{ijk} tensor can be described by only 18 independent elements and can be written as a 6×3 matrix using the same reduction of ij as given for jk in (7).

Table 3. Piezoelectric strain coefficients [$\times 10^{-11} \text{ C/N}$]

d_{15}	d_{22}	d_{31}	d_{33}	Ref.
6.92	2.08	-0.085	0.60	[24]
6.8	2.1	-0.1	0.6	[23]
7.4	2.1	-0.087	1.6	[25]

The application of Neumann's principle to the r_{ijk} tensor followed by the use of the reduced-subscript notation gives

$$r_{ijk} = \begin{bmatrix} 0 & -r_{22} & r_{13} \\ 0 & r_{22} & r_{13} \\ 0 & 0 & r_{33} \\ 0 & r_{42} & 0 \\ r_{42} & 0 & 0 \\ -r_{22} & 0 & 0 \end{bmatrix}. \quad (12)$$

Note that $r_{42}=r_{51}$, $r_{22}=-r_{12}=-r_{61}$, and $r_{13}=r_{23}$. This is analogous to the piezoelectric tensor elements with the subscripts reversed. Thus, the electro-optic effect in lithium niobate can be described by four independent coefficients (r_{51} , r_{22} , r_{13} , and r_{33}). The relative magnitudes of these coefficients are determined by the symmetry and relative orientation of the BO_6 octahedra in the crystal structure [37–39].

The measured values of these coefficients depend on the mechanical constraints imposed on the crystal. If the crystal is free (unclamped), the stress in the crystal is zero, if the crystal is rigidly held (clamped), the strain in the crystal is zero. In the free condition, the r coefficient value measured will also include a contribution from the secondary (or false) electro-optic effect. This secondary linear electro-optic effect is the result of the applied electric field causing a strain in the crystal through the converse piezoelectric effect. This electrically induced strain then causes a change in the crystal's refractive index through the photoelastic effect [Ref. 33, pp. 244–245]. Thus, to an observer who applies the electric field and is measuring the change in refractive index, this secondary contribution is inseparable from the primary linear electro-optic component. The relationship between the clamped coefficient (which is the primary linear electro-optic coefficient) and the unclamped coefficient can be written

$$r_{ij}^T = r_{ij}^S + p_{ik} d_{jk}, \quad 1 \leq k \leq 6, \quad (13)$$

where r_{ij}^T is the value measured at constant stress (free crystal), r_{ij}^S is the value measured at constant strain, p_{ik} is the photoelastic coefficient, and d_{jk} is the piezoelectric coefficient. A measurement made with a static applied electric field corresponds to the unclamped case. A measurement made with a high frequency (rf) electric field corresponds to the clamped condition and only the primary effect will be measured [Ref. 33, pp. 244–245]. Values for each of these coefficients are presented in Table 4. The values from [11] and [44] are probably the most accurate. These more recent values were obtained using refined experimental methods that correct for fringing fields present in previous measurements. Within the limits of experimental ac-

Table 4. Linear electro-optic coefficients [$\times 10^{-12}$ m/V]

Parameter	[nm]	r_{51}	r_{22}	r_{13}	r_{33}	Ref.
r^T	633	—	6.7	—	—	[40]
r^T	633	—	6.81 ^a	+10.0 ^a	+32.2 ^a	[37]
r^T	633	32	3.3 ^a	—	—	[41]
r^T	633	—	6.7	—	—	[42]
r^T	1150	—	5.4 ^a	—	—	[42]
r^T	3390	—	3.1	—	—	[42]
r^T	633	—	—	10.9	34.0	[42]
r^S	633	+18.2	—	—	—	[11]
r^S	633	—	+3.4	+7.7	+28.8	[44]
r^S	633	28	3.4	8.6	30.8	[45]
r^S	3390	23	3.1	6.5	28	[46]

^a These values were incorrect in [34]

curacy ($\pm 5\%$) there is no dependence of the free (unclamped) linear electro-optic coefficients on melt composition [28]. The temperature dependence of these coefficient values is linear and on the order of $5 \times 10^{-4}/^\circ\text{C}$ [13].

Theoretical investigations to determine the direction of the maximum magnitude of the linear electro-optic effect have been reported [39, 47]. Optimum directions for both phase- and polarization-modulated optical waves were reported in [47].

3.7. Elasticity

The elasticity of a solid can be described by the strain in the solid that results from an applied stress. Within the material's elastic limit, this relationship is linear and is represented by Hooke's law,

$$S_{ij} = \sum_{k,l} c_{ijkl} \sigma_{kl}, \quad (14)$$

where S_{ij} is the second-rank strain tensor and σ_{kl} is the second-rank stress tensor. Thus c_{ijkl} , the elastic stiffness tensor, is a fourth-rank tensor. A reciprocal expression can also be written as

$$\sigma_{ij} = \sum_{k,l} s_{ijkl} S_{kl}, \quad (15)$$

where s_{ijkl} is the elastic compliance, a fourth-rank tensor. If body torques are ignored it can be shown that $s_{ijkl} = s_{ijlk} = s_{jikl}$ and similarly, $c_{ijkl} = c_{ijlk} = c_{jikl}$ [Ref. 33, pp. 132–133]. Using these relations the reciprocal fourth-rank tensors (c and s) containing 81 elements are reduced to 36 independent elements that can be written as a 6×6 matrix using the index assignments given in (7). When this reduction is applied to the elastic compliance tensor the following assignments must also be made: $s_{ijkl} = s_{mn}$ when m and n are both 1, 2, or 3; $2s_{ijkl} = s_{mn}$ when m or n alone are 4, 5, or 6; and

$4s_{ijkl}=s_{mn}$ when m and n both are 4, 5, or 6 [Ref. 33, p. 134]. The application of Neumann's principle to the elastic compliance tensor followed by the use of the reduced-subscript notation gives the 6×6 matrix

$$s_{ijkl} = \begin{bmatrix} s_{11} & s_{12} & s_{13} & s_{14} & 0 & 0 \\ s_{12} & s_{11} & s_{13} & -s_{14} & 0 & 0 \\ s_{13} & s_{13} & s_{33} & 0 & 0 & 0 \\ s_{14} & -s_{14} & 0 & s_{44} & 0 & 0 \\ 0 & 0 & 0 & 0 & s_{44} & 2s_{14} \\ 0 & 0 & 0 & 0 & 2s_{14} & 2(s_{11}-s_{12}) \end{bmatrix}, \quad (16)$$

which applies to all crystals in the $3m$ point group. Note that the coefficient s_{56} was incorrectly labeled in [13]. Similarly, the elastic stiffness tensor can be represented by the 6×6 matrix

$$c_{ijkl} = \begin{bmatrix} c_{11} & c_{12} & c_{13} & c_{14} & 0 & 0 \\ c_{12} & c_{11} & c_{13} & -c_{14} & 0 & 0 \\ c_{13} & c_{13} & c_{33} & 0 & 0 & 0 \\ c_{14} & -c_{14} & 0 & c_{44} & 0 & 0 \\ 0 & 0 & 0 & 0 & c_{44} & c_{14} \\ 0 & 0 & 0 & 0 & c_{14} & \frac{1}{2}(c_{11}-c_{12}) \end{bmatrix}. \quad (17)$$

Each of the tensors contains only six independent coefficients. When determining the values of these coefficients, the contribution of the piezoelectric effect must be taken into account. Longitudinal components

Table 5. Elastic compliance coefficients [$\times 10^{-12} \text{ m}^2/\text{N}$] at constant electric field

Parameter	s_{11}	s_{12}	s_{13}	s_{14}	s_{33}	s_{44}	Ref.
s^E	5.831	-1.150	-1.452	-1.000	5.026	17.10	[24]
s^E	5.78	-1.01	-1.47	-1.02	5.02	17.0	[23]
s^E	5.64	-	-	-0.84	4.94	-	[25]
Normalized temperature coefficients ($\times 10^{-4}/^\circ\text{C}$)							
s^E	1.66	0.28	1.94	1.33	1.60	2.05	[24]
s^E	1.5	-	-	-	1.5	-	[25]

Table 6. Elastic stiffness coefficients [$\times 10^{11} \text{ N/m}^2$] at constant electric field

Parameter	c_{11}	c_{12}	c_{13}	c_{14}	c_{33}	c_{44}	Ref.
c^E	2.030	0.573	0.752	0.085	2.424	0.595	[24]
c^E	2.03	0.53	0.75	0.09	2.45	0.60	[23]
c^E	2.0	0.54	0.6	0.08	2.43	0.60	[27]
c^E	2.06 ± 0.03	-	-	-	2.36 ± 0.028	-	[36]
Normalized temperature coefficients ($\times 10^{-4}/^\circ\text{C}$)							
c^E	-1.74	-2.52	-1.59	-2.14	-1.53	-2.04	[24]

of elastic waves create corresponding longitudinal electric fields in the material which contribute additional stiffness terms [48, 49]. Measured values for the elastic compliance and elastic stiffness tensor coefficients and their temperature dependencies are given in Table 5 and 6. The effects of stoichiometry on these coefficients is not well known [13].

3.8. Photoelastic Effect

A change in the refractive index of a material as a result of a strain in the material is known as the photoelastic effect. The anisotropic photoelastic relationship between the strain and the refractive index is usually written

$$\Delta(1/n^2)_{ij} = \sum_{k,l} p_{ijkl} S_{kl}, \quad (18)$$

where $\Delta(1/n^2)_{ij}$ is the second-rank tensor describing the change in the relative permittivity of the material, S_{kl} is the second-rank strain tensor, and p_{ijkl} is the fourth-rank photoelastic (strain-optic) tensor. However, Nelson and Lax have shown that the independent elastic variable is not strain but instead is the displacement gradient [50]. Thus, rotation (of volume elements varying within an acoustic wavelength) as well as strain contributes to the change in refractive index of a material caused by acoustic shear waves. Therefore, the previously assumed symmetry of the photoelastic coefficients (corresponding to acoustic shear waves) upon the interchange of the two elastic indices is incorrect for anisotropic materials [51]. For lithium niobate, the photoelastic coefficients p_{44} and p_{55} , which are numerically equal, consist of symmetric and anti-symmetric components (with respect to the elastic indices) [51]. All other photoelastic coefficients contain only symmetric components.

Since the available data does not allow the resolution of the components of p_{44} , the interchange of elastic indices will be used here for ease of notation. In addition, as discussed previously, it can be shown that $\Delta(1/n^2)_{ij} = \Delta(1/n^2)_{ji}$ [Ref. 33, p. 248]. Using these two relations the fourth-rank tensor containing 81 elements is reduced to 36 independent elements that can

Table 7. Photoelastic (strain) coefficients [dimensionless] at constant electric field

p_{11}	p_{33}	p_{44}	p_{12}	p_{13}	p_{14}	p_{31}	p_{41}	Ref.
0.036	0.066	—	0.072	0.135	—	0.178	0.155	[54]
0.025	0.068	—	0.079	0.132	0.1 ^a	0.168	0.158	[55]
0.034	0.060	0.30 ^a	0.072	0.139	0.066	0.178	0.154	[56]
—	0.069	0.152	0.088	0.126	0.080	0.176	0.134	[53]
0.045 ^a	0.076 ^a	0.019	0.096	0.149	0.055	0.138	—	[57]
−0.026	+0.071	+0.146	+0.090	+0.133	−0.075	+0.179	−0.151	[52]
−0.02	+0.07	+0.12	+0.08	+0.13	−0.08	+0.17	−0.15	[58]

^a These values were incorrect in [34, 52]

be written as a 6×6 matrix using the assignments given by (7). The application of Neumann's principle to the \tilde{p} tensor followed by the use of the reduced-subscript notation gives the 6×6 matrix

$$p_{ijkl} = \begin{bmatrix} p_{11} & p_{12} & p_{13} & p_{14} & 0 & 0 \\ p_{12} & p_{11} & p_{13} & -p_{14} & 0 & 0 \\ p_{31} & p_{31} & p_{33} & 0 & 0 & 0 \\ p_{41} & -p_{41} & 0 & p_{44} & 0 & 0 \\ 0 & 0 & 0 & 0 & p_{44} & p_{41} \\ 0 & 0 & 0 & 0 & p_{14} & \frac{1}{2}(p_{11} - p_{12}) \end{bmatrix}. \quad (19)$$

Note this tensor contains only eight independent coefficients p_{11} , p_{12} , p_{13} , p_{14} , p_{31} , p_{33} , p_{41} , and p_{44} . When determining the values of these coefficients the contribution of the secondary (indirect) photoelastic effect must also be taken into account. As discussed previously, a secondary effect manifests itself just like the primary effect but is actually the coupling of two other effects. In this case, the applied strain causes an electric field through the piezoelectric effect. This electric field then causes a change in the crystal's refractive index through the linear electro-optic effect [52]. Thus, to the observer who applied the strain and is measuring the change in the refractive index, this secondary contribution is inseparable from the primary photoelastic effect. This indirect photoelastic effect can not be represented as an ordinary tensor but instead must be expressed as a tensor that is dependent on acoustic wave direction [50]. In lithium niobate, the secondary effect is significant in the determination of the values of p_{13} and p_{33} . The relationships between the measured coefficients and those describing the primary effect are [53]: $p_{13}(\text{pri}) = p_{13}(\text{meas}) - 0.043$, and $p_{33}(\text{pri}) = p_{33}(\text{meas}) - 0.154$. These relationships are consistent with the coefficient values given in Tables 3 and 4. Measured values for the photoelastic coefficients are given in Table 7.

To compare the usefulness of acousto-optical materials [59] for device applications various figures

of merit have been developed [60]. Four of these are:

$$\begin{aligned} M_1 &= n^7 p^2 / \rho v, & M_2 &= n^6 p^2 / \rho v^3, \\ M_3 &= n^7 p^2 / \rho v^2, & M_4 &= n^8 p^2 v / \rho, \end{aligned} \quad (20)$$

(n : average refractive index, p : applicable photoelastic coefficient, ρ : bulk mass density, and v : bulk acoustic wave velocity being $(qs)^{-1/2}$ where s is the applicable elastic compliance coefficient). M_1 is proportional to the product of the bandwidth and diffraction efficiency associated with a bulk acoustic wave for a given level of acoustic power if the height of the acoustic beam is constant [61]. It is appropriately used to select materials for devices such as modulators requiring optimum efficiency and bandwidth. M_2 is proportional to the diffraction efficiency associated with a bulk acoustic wave for a given level of acoustic power and is appropriately used to select materials for narrow-band devices [62]. M_3 is proportional to the diffraction efficiency associated with a bulk acoustic wave for a given level of acoustic power if the acoustic beam height can be made as small as the optical beam size in the wave interaction region [54]. M_4 is proportional to the product of the square of the bandwidth and the diffraction efficiency associated with a bulk acoustic wave for a given acoustic power density. It is appropriately used to select materials for wide-band applications where power density is the limiting factor [60]. For a longitudinal bulk acoustic wave propagating in the x -direction, and $n=2.20$, $\rho=4.7 \times 10^3 \text{ kg/m}^3$, $v=6.57 \times 10^3 \text{ m/s}$, and an optical beam extraordinarily polarized at an angle of 35° relative to the y -axis (measured in the y - z plane) the following typical values of the figures of merit have been reported for lithium niobate: $M_1=6.65 \times 10^{-7} \text{ m}^2 \text{ s kg}^{-1}$ [54], $M_2=6.99 \times 10^{-15} \text{ s}^3 \text{ kg}^{-1}$ [54], $M_3=1.01 \times 10^{-16} \text{ m s}^2 \text{ kg}$ [54], and $M_4=62.9 \text{ m}^4 \text{ s}^{-1} \text{ kg}^{-1}$ [60].

3.9. Bulk Photovoltaic Effect

The bulk photovoltaic effect is manifested as a short-circuit current through a solid that is uniformly

illuminated. It was first described as a new photovoltaic effect by Glass et al. in 1974 [63]. The bulk photovoltaic effect [64] is sometimes called the "anomalous photovoltage" or the "photogalvanic effect". The tensor relationship between the short-circuit current density and the illumination can be written

$$J_i = \sum_{jk} \alpha_{ijk} E_j E_k^*, \quad (21)$$

where J_i is the current density vector, E_j and E_k are components of the light complex electric field vector, α_{ijk} is the third-rank photovoltaic tensor (27 elements), and * represents complex conjugation. Since $E_j E_k^* = E_k^* E_j$, the α_{ijk} tensor can be described by only 18 independent elements and can be written as a 3×6 matrix using the reduction of jk as given in (7). The application of Neumann's principle to the α_{ijk} tensor followed by the use of the reduced-subscript notation gives

$$\alpha_{ijk} = \begin{bmatrix} 0 & 0 & 0 & 0 & \alpha_{15} & -2\alpha_{22} \\ -\alpha_{22} & \alpha_{22} & 0 & \alpha_{15} & 0 & 0 \\ \alpha_{31} & \alpha_{31} & \alpha_{33} & 0 & 0 & 0 \end{bmatrix}. \quad (22)$$

Note that $\alpha_{15} = \alpha_{24}$, $\alpha_{22} = -\alpha_{21} = -\alpha_{16}/2$, and $\alpha_{31} = \alpha_{32}$. Thus, the bulk photovoltaic effect in lithium niobate can be described by four independent coefficients α_{15} , α_{22} , α_{31} , and α_{33} . These coefficients for iron-doped lithium niobate at a free-space wavelength of 500 nm may be obtained from the experimental data of Fridkin and Magomadov [65]. The values are: $\alpha_{22} = 1.5 \times 10^{-10}$ A/W, $\alpha_{31} = 6 \times 10^{-9}$ A/W, and $\alpha_{33} = 6.8 \times 10^{-9}$ A/W. Although a value of α_{15} is indicated in [65], subsequent papers by Fridkin [66] and others [67] have shown that α_{15} could not be determined by the measurements reported in [65]. Festl et al. reconfirmed the tensor nature of the bulk photovoltaic effect and measured tensor coefficients in both iron-doped and copper-doped lithium niobate [67].

Microscopic quantities associated with the bulk photovoltaic effect such as the probability of creating a free electron and the mean migration length of an electron have been reported in [68].

3.10. Photorefractive "Effect"

Optically induced changes in optical absorption (color) have been referred to as the photochromic effect for many years. By analogy, optically induced changes in the refractive index are now commonly referred to as the photorefractive effect. The photorefractive "effect" is not strictly a single effect; it is a combination of effects. It is produced by a two step process: charge migration followed by an electro-optic effect (linear and/or quadratic). The charge migration may be produced by (a) diffusion, (b) drift, (c) bulk photovoltaic effect, or (d) a combination of these effects. In

lithium niobate the dominant charge migration mechanism is the bulk photovoltaic effect and the dominant electro-optic effect is the linear (Pockels) effect.

4. Summary

Lithium niobate is a very significant material for optical applications. It is a ferroelectric crystal that exhibits large birefringent, pyroelectric, piezoelectric, electro-optic, elastic, photoelastic, and bulk photovoltaic effects. In this paper, the standard orientation of the x , y , z principal axes used for describing the tensor physical properties was presented relative to the crystal structure. Applying the symmetry operations associated with the $3m$ crystal class together with other physical arguments, the forms of the resulting tensors were given explicitly for each effect. Measured values of the tensor elements for each effect were compiled and errors in the literature were corrected.

The two possible unit cells (hexagonal and rhombohedral) were clarified and shown on a common diagram. The translation vectors a_1 , a_2 , a_3 (equivalent to a_H), c , and a_R were shown. Three methods of determining the positive sense of the c axis (based on piezoelectric effect, pyroelectric effect, and crystal cleavage) were reviewed. All of the dimensions specifying the unit cells as determined by x-ray diffraction analysis were given.

Acknowledgement. This work was sponsored by the National Science Foundation and the Joint Services Electronics Program.

References

1. B.T. Matthias, J.P. Remeika: *Phys. Rev.* **76**, 1886–1887 (1949)
2. K. Nassau, H.J. Levinstein, G.M. Loiacono: *J. Chem. Phys. Solids* **27**, 983–988 (1966)
3. K. Nassau, H.J. Levinstein, G.M. Loiacono: *J. Chem. Phys. Solids* **27**, 989–996 (1966)
4. S.C. Abrahams, J.M. Reddy, J.L. Bernstein: *J. Chem. Phys. Solids* **27**, 997–1012 (1966)
5. S.C. Abrahams, W.C. Hamilton, J.M. Reddy: *J. Chem. Phys. Solids* **27**, 1013–1018 (1966)
6. S.C. Abrahams, W.C. Hamilton, J.M. Reddy: *J. Chem. Phys. Solids* **27**, 1019–1026 (1966)
7. S.C. Abrahams, E. Buehler, W.C. Hamilton, S.J. Laplace: *J. Chem. Phys. Solids* **34**, 521–532 (1973)
8. B.K. Vainshtein: *Modern Crystallography I*, Springer Ser. Solid-State Sci. **15** (Springer, Berlin, Heidelberg 1981)
9. *Proc. IRE* **37**, 1378–1395 (1949)
10. G.D. Boyd, R.C. Miller, K. Nassau, W.L. Bond, A. Savage: *Appl. Phys. Lett.* **5**, 234–236 (1964)
11. I.P. Kaminow, E.H. Turner, R.L. Barns, J.L. Bernstein: *J. Appl. Phys.* **51**, 4379–4384 (1980)
12. B.D. Cullity: *Elements of X-ray Diffraction* (Addison-Wesley, Reading, MA 1978) pp. 504–505
13. A. Rauber (E. Kaldis, ed.): *Current Topics Mat. Sci.* **1**, 481–601 (North-Holland, Amsterdam 1978)
14. P. Lerner, C. Legras, J.P. Duman: *J. Cryst. Growth* **3/4**, 231–235 (1968)

15. J.R. Carruthers, G.E. Peterson, M. Grasso, P.M. Bridenbaugh: J. Appl. Phys. **42**, 1846–1851 (1971)
16. J.G. Bergman, A. Ashkin, A.A. Ballman, J.M. Dziedzic, H.J. Levinstein, R.G. Smith: Appl. Phys. Lett. **12**, 92–94 (1968)
17. H.D. Megaw: Acta Cryst. **A24**, 589–604 (1968)
18. K. Sugii, H. Koizumi, S. Miyazawa, S. Kondo: J. Cryst. Growth **33**, 199–202 (1976)
19. Y.S. Kim, R.T. Smith: J. Appl. Phys. **40**, 4637–4641 (1969)
20. J.S. Browder, S.S. Ballard: Appl. Opt. **16**, 3214–3217 (1977)
21. e. g., Crystal Technology, Inc., 2510 Old Middlefield Way, Mountain View, CA 94040, USA
22. A. Savage: J. Appl. Phys. **37**, 3071–3072 (1966)
23. A.W. Warner, M. Onoe, G.A. Coquin: J. Acoust. Soc. Am. **42**, 1223–1231 (1967)
24. R.T. Smith, F.S. Welsh: J. Appl. Phys. **42**, 2219–2230 (1971)
25. T. Yamada, N. Niizeki, H. Toyoda: Jpn. J. Appl. Phys. **6**, 151–155 (1967)
26. J.R. Teague, R.R. Rice, R. Gerson: J. Appl. Phys. **46**, 2864–2866 (1975)
27. Y. Nakagawa, K. Yamanouchi, K. Shibayama: J. Appl. Phys. **44**, 3969–3974 (1973)
28. E.H. Turner, F.R. Nash, P.M. Bridenbaugh: J. Appl. Phys. **41**, 5278–5281 (1970)
29. D.F. Nelson, R.M. Mikulyak: J. Appl. Phys. **45**, 3688–3689 (1974)
30. G.D. Boyd, W.L. Bond, H.L. Carter: J. Appl. Phys. **38**, 1941–1943 (1967)
31. D.S. Smith, H.D. Riccius, R.P. Edwin: Opt. Commun. **17**, 332–335 (1976) Also Erratum **20**, 188 (1977)
32. G.J. Edwards, M. Lawrence: Opt. Quantum Electron. **16**, 373–374 (1984)
33. J.F. Nye: *Physical Properties of Crystals* (Oxford U. Press, Oxford 1957) p.115
34. T. Yamada (K.-H. Hellwege, ed.): *Landolt-Börnstein Numerical Data and Functional Relationships in Science and Technology, New Series, Group III, Vol. 16a* (Springer, Berlin, Heidelberg 1981) pp.149–156 and pp.489–499
35. R.A. Graham: Ferroelectr. **10**, 65–69 (1976)
36. R.A. Graham: J. Appl. Phys. **48**, 2153–2163 (1977)
37. J.D. Zook, D. Chen, G.N. Otto: Appl. Phys. Lett. **11**, 159–161 (1967)
38. M. DiDomenico, Jr., S.H. Wemple: J. Appl. Phys. **40**, 720–752 (1969)
39. A.A. Bereznoi: Opt. Spectrosc. **49**, 178–181 (1980)
40. P.V. Lenzo, E.G. Spencer, K. Nassau: J. Opt. Soc. Am. **56**, 633–635 (1966)
41. E. Bernal, G.D. Chen, T.C. Lee: Phys. Lett. **21**, 259–260 (1966)
42. P. H. Smakula, P.C. Claspy: Trans. Metall. Soc. AIME **239**, 421–424 (1967)
43. K. Onuki, N. Uchida, T. Saku: J. Opt. Soc. Am. **62**, 1030–1032 (1972)
44. E.H. Turner cited in [11]
45. E.H. Turner: Appl. Phys. Lett. **8**, 303–304 (1966)
46. E.H. Turner: J. Opt. Soc. Am. **56**, 1426 (1966)
47. A.A. Blistanov, N.V. Perelomova, L.E. Chirkov, V.A. Shkitin: Sov. Phys.-Cryst. **24**, 287–291 (1979)
48. A.R. Hutson, D.L. White: J. Appl. Phys. **33**, 40–47 (1962)
49. J.J. Kyame: J. Acoust. Soc. Am. **21**, 159–167 (1949)
50. D.F. Nelson, M. Lax: Phys. Rev. **B3**, 2778–2794 (1971) Also Erratum Phys. Rev. **B4**, 3779 (1971)
51. D.F. Nelson, M. Lax: Phys. Rev. Lett. **24**, 379–380 (1970)
52. L.P. Avakyants, D.F. Kiselev, N.N. Shchitkov: Sov. Phys.-Solid State **18**, 899–901 (1976)
53. L. Marlescu, G. Hauret: Compt. Rend. Acad. Sci. (B) **276**, 555–558 (1973)
54. R.W. Dixon: J. Appl. Phys. **38**, 5149–5153 (1967)
55. V.V. Lemanov, O.V. Shakin, G.A. Smolenskii: Sov. Phys.-Solid State **13**, 426–428 (1971)
56. R.J. O'Brien, G.J. Rosasco, A. Weber: J. Opt. Soc. Am. **60**, 716 (1970)
57. V.V. Kludzin: Sov. Phys.-Solid State **13**, 540–541 (1971)
58. G.A. Coquin cited in D.A. Pinnow: *Handbook of Lasers with Selected Data on Optical Technology*, ed. by R.J. Pressley, (Chemical Rubber, Cleveland 1971) p.482
59. A.A. Oliner (ed.): *Acoustic Surface Waves*, Topics Appl. Phys. **24** (Springer, Berlin, Heidelberg 1978) Chap. 6
60. I.C. Chang: IEEE Trans. SU-**23**, 2–22 (1976)
61. E.I. Gordon: IEEE J. QE-**2**, 104–105 (1966)
62. T.M. Smith, A. Korpel: IEEE J. QE-**1**, 283–284 (1965)
63. A.M. Glass, D. von der Linde, T.J. Negran: Appl. Phys. Lett. **25**, 233–235 (1974)
64. H.M. Smith (ed.): *Holographic Recording Materials*, Topics Appl. Phys. **20** (Springer, Berlin, Heidelberg 1977) Chap.4
65. V.M. Fridkin, R.G. Magomadov: JETP Lett. **30**, 686–688 (1979)
66. V.M. Fridkin: Ferroelectr. **53**, 169–187 (1984)
67. H.G. Festl, P. Hertel, E. Kratzig, R. von Baltz: Phys. Stat. Sol. **B113**, 157–164 (1982)
68. R. Grousson, M. Henry, S. Mallick, S.L. Xu: J. Appl. Phys. **54**, 3012–3016 (1983)